



Article

Ti Porous Film-Supported NiCo₂S₄ Nanotubes Counter Electrode for Quantum-Dot-Sensitized Solar Cells

Jianping Deng ^{1,*}, Minqiang Wang ^{2,*}, Xiaohui Song ³, Zhi Yang ² and Zhaolin Yuan ¹

¹ Shaanxi Key Laboratory of Industrial Automation, School of Physics and Telecommunication Engineering, Shaanxi University of Technology, Hanzhong 723001, China; yuanzhaolin98@126.com

² Electronic Materials Research Laboratory, Key Laboratory of the Ministry of Education & International Center for Dielectric Research, School of Electronic and Information Engineering, Xi'an Jiaotong University, Xi'an 710049, China; yangzhi029@xjtu.edu.cn

³ Henan Key Laboratory of Photovoltaic Materials, College of Physics and Materials Science, Henan Normal University, Xinxiang 453000, China; songsxh@126.com

* Correspondence: jpdeng0214@163.com (J.D.); mqwang@mail.xjtu.edu.cn (M.W.); Tel.: +86-(0)91-6264-1715 (J.D.); +86-(0)29-8266-8794 (M.W.)

Received: 22 March 2018; Accepted: 13 April 2018; Published: 17 April 2018



Abstract: In this paper, a novel Ti porous film-supported NiCo₂S₄ nanotube was fabricated by the acid etching and two-step hydrothermal method and then used as a counter electrode in a CdS/CdSe quantum-dot-sensitized solar cell. Measurements of the cyclic voltammetry, Tafel polarization curves, and electrochemical impedance spectroscopy of the symmetric cells revealed that compared with the conventional FTO (fluorine doped tin oxide)/Pt counter electrode, Ti porous film-supported NiCo₂S₄ nanotubes counter electrode exhibited greater electrocatalytic activity toward polysulfide electrolyte and lower charge-transfer resistance at the interface between electrolyte and counter electrode, which remarkably improved the fill factor, short-circuit current density, and power conversion efficiency of the quantum-dot-sensitized solar cell. Under illumination of one sun (100 mW/cm²), the quantum-dot-sensitized solar cell based on Ti porous film-supported NiCo₂S₄ nanotubes counter electrode achieved a power conversion efficiency of 3.14%, which is superior to the cell based on FTO/Pt counter electrode (1.3%).

Keywords: NiCo₂S₄ nanotubes; Ti porous film; quantum dot; solar cells; counter electrode

1. Introduction

In recent years, the quantum-dot-sensitized solar cell (QDSSC) has aroused a widespread attention due to the large absorption coefficient, multiple exciton generation, and the tunable absorption spectrum based on quantum confinement effect. QDSSC is composed of three parts: QD-sensitized TiO₂ or ZnO photoanode, electrolyte (S_n²⁻/S²⁻), and counter electrode (CE) [1]. As one of the most important parts in QDSSC, CE is used as a catalyst to reduce S_n²⁻/S²⁻ after the electron injection from external circuit so that QD can be regenerated. For achieving this function, CE materials should provide superior catalytic activity and high chemical stability against the corrosive polysulfide electrolyte.

As is well known, Pt is a poor electrocatalyst for reducing S_n²⁻/S²⁻ due to its strong chemisorption with S²⁻ ions, resulting in the serious corrosion and much higher overpotentials for electrolyte regeneration. Therefore, the QDSSC with Pt CE show a low fill factor (FF) and power conversion efficiency (PCE) [2], and the high cost is another disadvantage. Recently, some Pt-free CE materials with low cost, such as carbon materials [3–5], conductive polymers [6], and inorganic compound [7], have been widely developed and demonstrated to have attractive

performances. Of these Pt-free CE materials, the transition-metal sulfides, such as CuS, FeS, CoS, NiS, and NiCo₂S₄ [8–12], have attracted tremendous interest. Especially, NiCo₂S₄ contains higher electrochemical characteristics compared with binary NiS and CoS. NiCo₂S₄ has been regarded as one of the most potential electrode materials for a super-capacitor for are several main reasons, as follows: (1) NiCo₂S₄ has a high electric conductivity, which is approximately 100 times higher than that of NiCo₂O₄ and higher than that of NiS and CoS [13]; (2) NiCo₂S₄ has good mechanical and thermal stability and two different metal cations (Co and Ni) supplying richer redox reactions, leading to better electrochemical performance [14–17]. Up until now, NiCo₂S₄ as an efficient CE has also been widely used in dye-sensitized solar cell (DSSC). Shi et al. reported that NiCo₂S₄ nanosheet films were used as a CE of DSSC, the photocurrent density is increased by 3 mA/cm² [18]. Huo et al. fabricated the flower-like NiCo₂S₄/NiS micro-spheres, then the NiCo₂S₄/NiS was coated on FTO (fluorine doped tin oxide) conductive glass as a CE for DSSC and the PCE of DSSC increased by 8.24% compared with that of the DSSC based on Pt CE [19]. A compact NiCo₂S₄ film with a thickness of 40 nm and a cross-linked network of NiCo₂S₄ nanosheet film coated FTO conductive glass were used as CEs for DSSC [20,21], and the DSSC with NiCo₂S₄ CE exhibited higher PCE compared with that of Pt CE-based DSSC. In addition, one-dimensional (1D) nanomaterials (e.g., nanorod, nanowire, nanotube) with direct electrical pathways show excellent application prospects in nanoscale electronic devices. One-dimensional NiCo₂S₄ nanotube arrays were used for supercapacitors [22] and 1D Co₉S₈ hollow nanoneedle arrays were used as CE for QDSSC [11].

The substrate supporting CE materials is also very important for the performance of DSSC; it should have large surface area, excellent conductivity, and good corrosion resistance to the electrolyte. Owing to the poor conductivity of metal sulfides, improving the catalytic activity of CE by increasing the thickness of CE is limited. In order to solve this problem, the porous microstructure with a large surface is used to load CE materials. For example, porous SnO₂, ZnO, TiO₂, and carbon and nickel foam were used as catalyst support [7,9,23,24]. The porous Cu₂S and FeS CEs were directly prepared on Cu and Fe substrates by in situ corrosion method [25], but they can easily peeled off from the substrates because of the reaction of Cu and Fe substrates with S²⁻ in electrolyte. In addition, it is important that the electrons from the external circuit quickly transfer to CE materials and reduce the electrolyte. So far, various substrates have been used, such as FTO and ITO (indium doped tin oxide) conductive glass [3–6], C fiber cloth and C paper [16], Ti mesh [26], and abovementioned Fe and Cu. Generally, two methods are available to prepare CE: one is the in situ growth method, the other is the ex situ coating method. For the former, there is a good adhesion between the substrate and CE materials, but the load of CE materials is limited. For the latter, although CE materials can be increased by increasing the coating several times, the adhesion is poor. In order to solve the adhesion problem, the adhesive was added into the CE materials [27], but it increased the electron transfer resistance.

In this paper, we have designed NiCo₂S₄ nanotubes supported on Ti porous film (Ti-PF) as CE for QDSSC. Firstly, Ti-PF was prepared by acid etching, then NiCo₂S₄ nanotubes were synthesized on Ti-PF by two-step hydrothermal method. NiCo₂S₄ nanotubes not only provide the effective path for electron transport but also have more electroactive sites for reducing polysulfide electrolyte. In addition, Ti-PF/NiCo₂S₄ CE exhibits lower charge-transfer resistance compared with FTO/Pt CE owing to the high conductivity of Ti and the porous structure increases the load of CE materials and improves the stability via the pore-wall. As a result, the PCE (3.14%) of QDSSC based on Ti-PF/NiCo₂S₄ CE is higher than that (1.3%) of QDSSC based on Pt CE.

2. Experimental Section

In this work, NiCo₂S₄ nanotubes supported on Ti-PF were prepared by the following three steps (Figure 1): (1) Ti-PF was prepared by acid etching as the substrates (Step 1); (2) Ni–Co precursor ((Ni,Co)₂(CO₃)(OH)₂) nanorods were hydrothermally grown (Step 2); and (3) (Ni,Co)₂(CO₃)(OH)₂ nanorods were converted into NiCo₂S₄ nanotubes in Na₂S solution via an anion-exchange reaction (Step 3).

2.1. Preparation of Ti-PF

Firstly, Ti sheets with high purity (TA1, 99.9%) and 0.2 mm thickness were washed in the acetone and ethanol using an ultrasonic bath for 30 min, respectively, and rinsed with deionized water. Then, the cleaned Ti sheets were immersed in 90 mL of HCl solution (25 wt-%) for 24–72 h at room temperature. Next, Ti-PF sheets were washed thoroughly with deionized water until the pH was close to 7 and further dried in air.

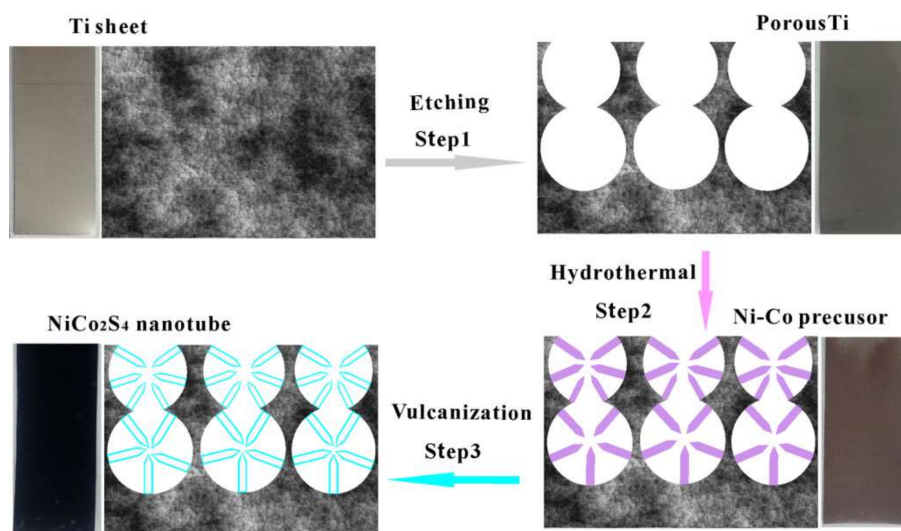


Figure 1. Schematic diagram to illustrate the preparation process of NiCo_2S_4 nanotubes on Ti porous film (Ti-PF).

2.2. Fabrication of NiCo_2S_4 Nanotubes

NiCo_2S_4 nanotubes were prepared by two-step hydrothermal method according to the literature [14,28]. All the reagents were of analytical grade in this experiment and purchased from Sinopharm (Beijing, China). Firstly, 4 mmol $\text{CoCl}_2 \cdot 6\text{H}_2\text{O}$, 2 mmol $\text{NiCl}_2 \cdot 6\text{H}_2\text{O}$, and 12 mmol urea were dissolved in 35 mL deionized water and stirred to form a pink homogeneous solution. Subsequently, the mixed-solution and Ti-PF sheets were transferred into 50 mL Teflon-lined stainless-steel autoclave and then heated at 120 °C for 10 h. After being cooled to room temperature, Ti-PF sheets with pink product were washed with deionized water and ethanol and then dried at 60 °C in air for 10 h. The $(\text{Ni},\text{Co})_2(\text{CO}_3)(\text{OH})_2$ nanorods were obtained. In the next step, the $(\text{Ni},\text{Co})_2(\text{CO}_3)(\text{OH})_2$ was transformed into NiCo_2S_4 by a hydrothermal process in 0.1 M $\text{Na}_2\text{S} \cdot 9\text{H}_2\text{O}$ solution at 120 °C for 10 h. After being cooled to room temperature, Ti-PF sheets with black products were washed with deionized water and ethanol and then dried in air at 60 °C. The NiCo_2S_4 nanotube CE was obtained.

2.3. Assembly of QDSSCs

The QDSSC was fabricated using a screen printing technique with the home-made TiO_2/ZnO paste [29]. Firstly, the TiO_2 compact layer was prepared via a spin-coating method and followed by calcination at 400 °C for 0.5 h. Subsequently, the mesoscopic photoanodes were prepared through four circulars screen printing of TiO_2/ZnO paste on FTO conductive glass with TiO_2 compact layer and sintered at 450 °C for 0.5 h. The active area of the film is 0.25 cm². Next, the growth of ZnO nanowires was performed in a procedure similar to that in our previous paper. Lastly, CdS/CdSe/ZnS QDs were deposited by successive ionic layer adsorption and reaction (SILAR) method [1,29]. A polysulfide electrolyte used in the QDSSCs and the symmetric cells was prepared by dissolving 1 M Na_2S , 1 M S and 0.2 M KCl in a methanol/water solution (7:3, v/v).

2.4. Characterization and Measurements

Field emission scanning electron microscopy (FE-SEM, S-4800, Hitachi, Tokyo, Japan) and transmission electron microscope (TEM, Tecnai G2F20, FEI, Columbus, OH, USA) were carried out to investigate the morphology and composition. The X-ray diffraction (XRD) patterns were obtained by D/max-2400 X-ray diffraction spectrometer (Rigaku, Akishima-Shi, Japan) with Cu K α radiation at 40 kV and 100 mA. The current-voltage (I-V) characterization was performed under AM 1.5 G simulated sunlight (100 mW/cm²) and recorded by a Keithley 2400 Source Meter (Keithley Instruments, Inc., Cleveland, OH, USA). The cyclic voltammetry (CV), Tafel polarization curves, and electrochemical impedance spectroscopy (EIS) were performed in the symmetric cells on the workstation (CHI660E, CH Instruments Ins., Shanghai, China). These tests were used to investigate the electrocatalytic ability of CE towards the reduction of S_n²⁻/S²⁻ electrolyte and the electronic transport properties of CE. In CV tests, the scanning potential range is from -1.2 V to 1 V with a scan rate of 100 mV/s. EIS curves were recorded at bias voltage of 0 V over a frequency range of 0.1 Hz to 1 MHz with AC amplitude of 10 mV, all EIS spectra were analyzed by ZsimpWin software. Polarization Tafel curves were recorded from -0.6V to 0.6 V at the scan rate of 10 mV/s.

3. Results and Discussion

3.1. Morphology of Ti-PF

Figure 2 shows the SEM images for Ti-PF with different etching time in HCl. Generally, metal Ti is stable in low concentration of HCl at room temperature. However, Ti is slowly etched when HCl concentration is greater than 20%. In our experiment, HCl solution with concentration of 25% is used to etch Ti sheets at room temperature and the morphology of Ti-PF is controlled by adjusting the etching time. Figure 2a–f show the morphologies of Ti-PF with etching 24 h, 48 h, and 72 h, respectively. It can be seen clearly that with the increase of etching time, the porous structure has changed significantly. When the etching time is 24 h, the holes with the size range of about 5–10 μ m exist only in very few places (Figure 2a,b). When the etching time increases to 48 h, the holes with the size range of 10–20 μ m are uniformly formed on the surface of Ti sheet (Figure 2c,d). With an increase in etching time (up to 72 h), the holes disappeared completely (Figure 2e) and the shallow pits with the size of below 5 μ m were formed (Figure 2f). In this experiment, Ti-PF plays three roles to improve the catalytic activity of CE to polysulfide electrolyte: (1) metal Ti provides a fast electronic transmission channel, (2) the porous structure gives a large surface area and thus increases the load of CE materials, and (3) the deeper holes in which NiCo₂S₄ nanotubes are limited by the wall increase the stability of CE. Therefore, the Ti-PF etched for 48 h is most suitable for using as the CE substrate.

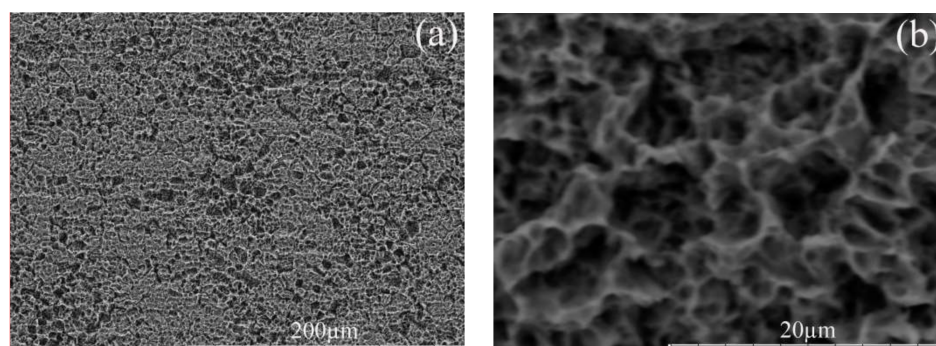


Figure 2. Cont.

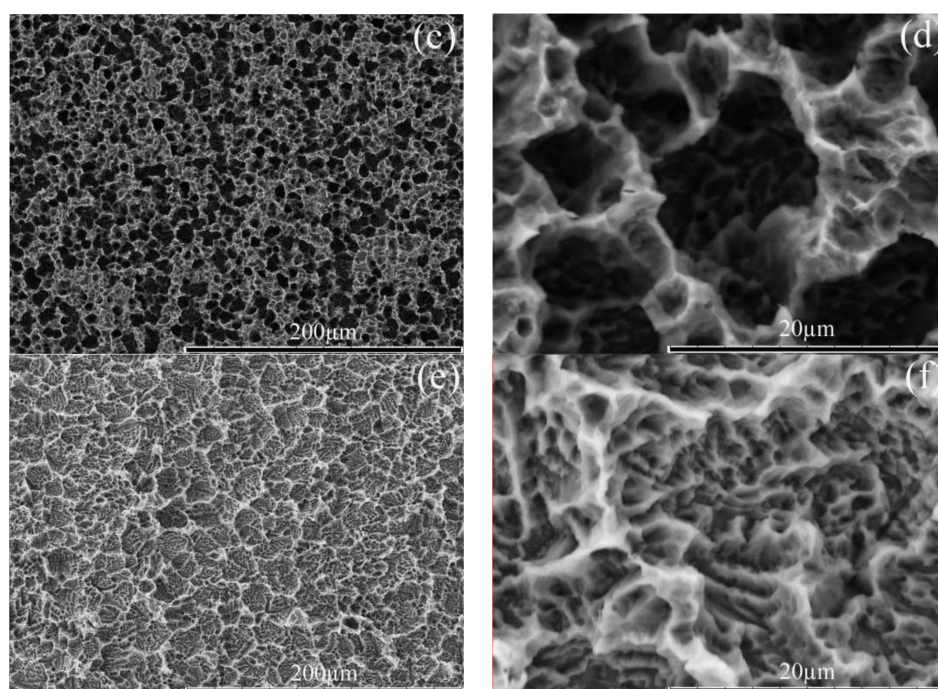


Figure 2. SEM images for Ti-PF from different etching time. (a,b)24 h, (c,d)48 h, and (e,f)72 h.

3.2. Morphology of NiCo_2S_4 Nanotubes

The conversion of $(\text{Ni,Co})_2(\text{CO}_3)(\text{OH})_2$ nanorods into NiCo_2S_4 nanotubes can be explained by the anion-exchange reaction mechanism [22,30,31]. Firstly, S^{2-} in the Na_2S solution exchanges with CO_3^{2-} and OH^- on the surface of $(\text{Ni,Co})_2(\text{CO}_3)(\text{OH})_2$ nanorods to form NiCo_2S_4 , CO_3^{2-} , and OH^- react with H^+ in the solution to produce CO_2 and H_2O . At the same time, the internal $(\text{Ni,Co})_2(\text{CO}_3)(\text{OH})_2$ diffuse spontaneously to the surface of the nanorod, where it provides a source of $(\text{Ni,Co})_2(\text{CO}_3)(\text{OH})_2$ for further anion exchange. The continuous outward diffusion results in the generation of void space inside the nanorod. When $(\text{Ni,Co})_2(\text{CO}_3)(\text{OH})_2$ has been completely converted into NiCo_2S_4 , nanorods become nanotubes.

To illustrate the morphology of as-synthesized samples, SEM measurements were performed. Figure 3a,b,e show the representative low-magnification and high-magnification SEM images of $(\text{Ni,Co})_2(\text{CO}_3)(\text{OH})_2$ nanorods, respectively. Figure 3c,b,f correspond to the low-magnification and high-magnification SEM images of NiCo_2S_4 nanotubes, respectively. In Figure 3a–d, $(\text{Ni,Co})_2(\text{CO}_3)(\text{OH})_2$ nanorods and NiCo_2S_4 nanotubes were homogeneously deposited on Ti-PF, suggesting that the two-hydrothermal method is favorable in forming this structure. Moreover, the NiCo_2S_4 nanotubes were well preserved during sulfurization process. It can be seen that the $(\text{Ni,Co})_2(\text{CO}_3)(\text{OH})_2$ array film is composed by many multi-directional nanorods due to the nucleation sites from the wall of holes and there is considerable inter-nanorod space, it will help electrolyte full contact with CE materials at the bottom, improving the utilization rate of the CE materials. A rough comparison between Figure 3b,d the diameters of NiCo_2S_4 nanotubes are larger than that of $(\text{Ni,Co})_2(\text{CO}_3)(\text{OH})_2$ nanorods, owing to the Ni and Co ions diffusion from inside to outside of the nanorod during an anion-exchange process. As shown in Figure 3e,f $(\text{Ni,Co})_2(\text{CO}_3)(\text{OH})_2$ nanorods with a smooth surface and solid structure and NiCo_2S_4 nanotubes with a rough surface are clearly seen from the damaged film.

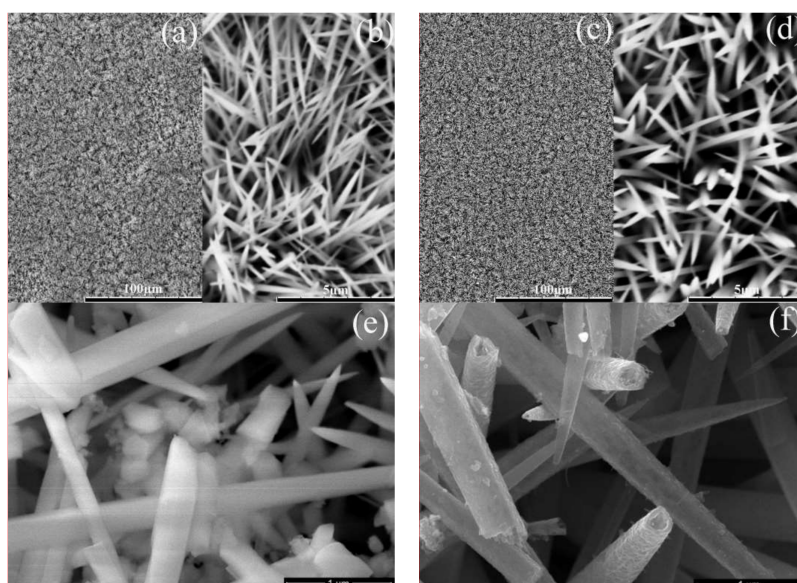


Figure 3. SEM images for $(\text{Ni,Co})_2(\text{CO}_3)(\text{OH})_2$ nanorods (a,b,e) and NiCo_2S_4 nanotubes (c,d,f) on Ti-PF.

The detailed structure of NiCo_2S_4 nanotube scraped from Ti-PF sheet was further confirmed by TEM, as shown in Figure 4. From Figure 4a, the nanotube structure and the porous wall can be evidently seen, indicating the successful preparation of NiCo_2S_4 nanotubes on Ti-PF. By a closer examination of the wall in Figure 4b, it is found that NiCo_2S_4 nanotube is composed of many nanoparticles with a size of about 25 nm (marked with red line) and numerous pores locate at the nanotube. The NiCo_2S_4 nanotube with a rough surface (Figure 4a–c) and a thin wall of about 25 nm (Figure 4c) effectively increases the electroactive sites. The nanotube structure can greatly enhance the electrolyte penetration and improve the performance of cells. In Figure 4c, the corresponding selected area electron diffraction (SAED) pattern indicates the polycrystalline nature of NiCo_2S_4 nanotubes and the diffraction rings can be readily indexed to the (111), (220), (311), (400), (511), and (440) planes of NiCo_2S_4 phase. In addition, Figure 4d reveals that the lattice spacings are about 0.51 nm, 0.284 nm, and 0.234 nm, which can be assigned to the (111), (311), and (400) crystal planes of the cubic NiCo_2S_4 phase, respectively, indicating the successful formation of crystalline NiCo_2S_4 .

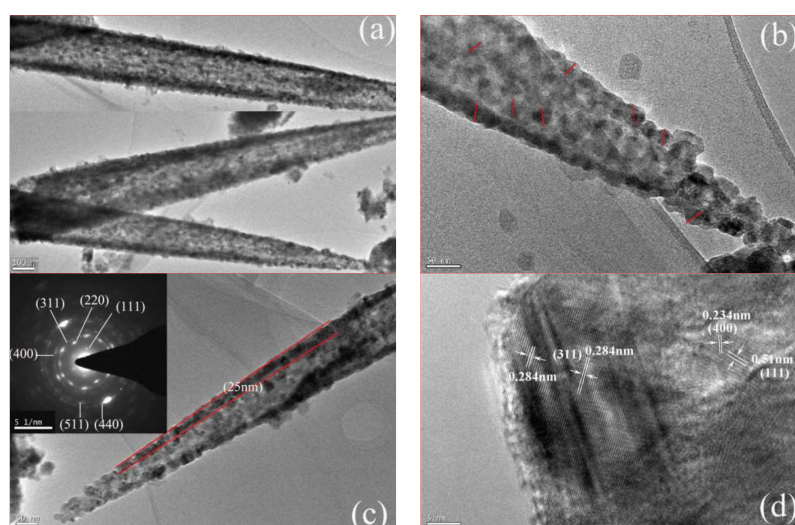


Figure 4. (a–c) TEM and (inset) SAED and (d) HRTEM images of NiCo_2S_4 nanotube.

The as-synthesized NiCo_2S_4 nanotubes were further confirmed by the XRD and electron energy loss spectroscopy (EELS) elemental mapping. In order to investigate the effect of annealing treatment on the catalytic activity of NiCo_2S_4 CE and the performance of cells, NiCo_2S_4 CE was annealed at 400°C for 30 min in the nitrogen atmosphere ($\text{NiCo}_2\text{S}_4\text{-an}$). Figure 5a shows XRD images for Ti-PF, NiCo_2S_4 , and $\text{NiCo}_2\text{S}_4\text{-an}$ on Ti-PF. The diffraction peaks located at 31.6° , 38.3° , 50.5° , and 55.3° can be indexed to the (311), (400), (511), and (440) planes of the cubic phase NiCo_2S_4 (JCPDS 20-0782), which is consistent with SAED analysis. There are also two strong peaks at 29.84° and 52.0° , which may correspond to the (311) and (440) planes of the cubic phase Co_9S_8 (JCPDS no.19-0364). The existence of Co_9S_8 phase is because that $(\text{Ni},\text{Co})_2(\text{CO}_3)(\text{OH})_2$ nanorods were incompletely sulfurized in Na_2S solution, which was verified by many reports [14,32]. It can also be seen that the intensity of (311) and (440) diffraction peaks of NiCo_2S_4 increased after annealing, indicating an increase in the crystallinity. Moreover, the TEM and EELS mapping images (Figure 5b) indicate that the elements (Ni, Co, and S) are uniformly distributed in the NiCo_2S_4 nanotube.

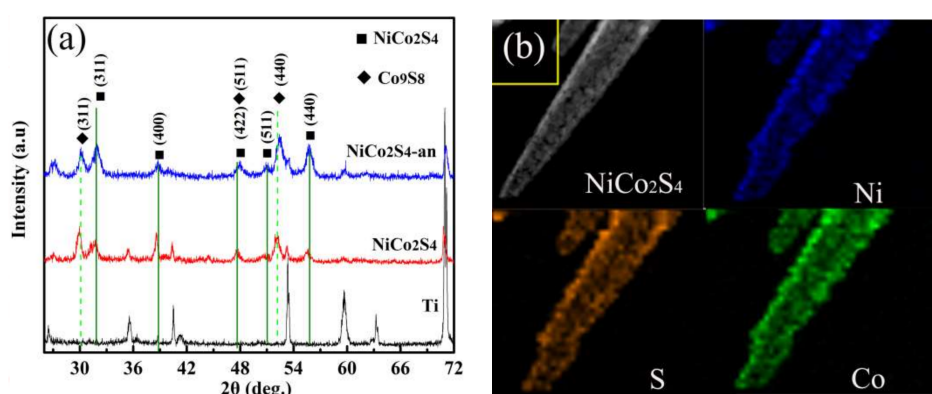


Figure 5. (a) XRD images for Ti-PF, NiCo_2S_4 , and $\text{NiCo}_2\text{S}_4\text{-an}$ on Ti-PF; (b) TEM image and the corresponding EELS elemental mapping images of a single NiCo_2S_4 nanotube.

3.3. Electrochemical Properties of CEs

To investigate the electrochemical properties of Pt, NiCo_2S_4 , and $\text{NiCo}_2\text{S}_4\text{-an}$ CEs, CV test of a symmetrical cell was carried out, as shown in Figure 6a. The peaks explain the catalytic reaction at the interface between CE and electrolyte as follows $\text{S}_n^{2-} + e^- \rightarrow \text{nS}^{2-}$. From the CV curves, NiCo_2S_4 and $\text{NiCo}_2\text{S}_4\text{-an}$ CEs present a similar shape with two typical pairs of redox peaks [16,21]. As a matter of fact, the reduction peak of the left pair is assigned to the reaction $\text{S}_n^{2-} + e^- \rightarrow \text{nS}^{2-}$ and the right one is assigned as $\text{S} + 2\text{ne}^- \rightarrow \text{S}_n^{2-}$ [19,20,33]. The role of the CE in a QDSSC is to catalyze the reduction of S_n^{2-} to S^{2-} ions in the polysulfide electrolyte, so the left pair of redox peaks is directly related to the catalytic activity of CE, the positive and negative peaks correspond to the oxidation of S^{2-} and the reduction of S_n^{2-} , respectively [34,35]. However, because of high over-potential, Pt CE has only one pair of redox peaks, which correspond to the oxidation of S^{2-} and the reduction of S_n^{2-} [36]. The higher current density of left cathodic peak indicates that the CE has an excellent electrocatalytic activity for the reduction of S_n^{2-} to nS^{2-} [17]. It can be seen that NiCo_2S_4 and $\text{NiCo}_2\text{S}_4\text{-an}$ CEs show higher current than Pt CE and the reduction current density of $\text{NiCo}_2\text{S}_4\text{-an}$ CE is the biggest. This results indicate that the NiCo_2S_4 CE is expected to enhance QD regeneration and photoelectron generation, thus beneficial for improving QDSSC's photocurrent, and the annealing treatment enhanced the crystallinity of NiCo_2S_4 CE, which increases the reduction current.

Tafel polarization technique is an important method to evaluate the catalytic activity of CEs. Theoretically, the Tafel curve includes the diffusion, Tafel and polarization zones at the high-, middle-, and low-potential areas, respectively. In Tafel analysis, the exchange current density (J_0) (Tafel zone) and the limiting diffusion current density (J_{lim}) (diffusion zone) are two key parameters to evaluate

the electrocatalytic activity of CEs. Tafel polarization curves of Pt, NiCo₂S₄, and NiCo₂S₄-an CEs are shown in Figure 6b. It can be seen that, in the Tafel zone, the slopes of the anodic or cathodic branches are in the order of NiCo₂S₄-an > NiCo₂S₄ > Pt. A larger slope indicates a higher J_0 . According to the following equation:

$$J_0 = RT/nFR_{ct}, \quad (1)$$

where R , T , F and n are the gas constant, the temperature, Faraday's constant, and the electron number involved in Sn²⁺/S²⁻ redox couple, respectively [35]; the charge-transfer resistance (R_{ct}) can be calculated by J_0 values. The change trends of the R_{ct} is NiCo₂S₄-an < NiCo₂S₄ < Pt, which is consistent with the EIS results. In addition, J_{lim} derived from the horizontal part of the curve at high potential is also closely related to the catalytic activity of CEs, which is given by equation:

$$D = L J_{lim}/2nFC, \quad (2)$$

where D , L , F , C , and n are the diffusion coefficient of the polysulfide, the electrolyte thickness, the Faraday constant, the polysulfide concentration, and the number of electrons involved in the reduction of disulphide at the counter electrode, respectively [37]. It can be noticed that the change trend of J_{lim} is consistent with CV results, suggesting the D of redox couple in the electrolyte increases with enhanced electrocatalytic activity of CEs.

To further understand the reason for the good performance of the as-prepared CEs, EIS was carried out using the symmetrical cells, as shown in Figure 6c, and the corresponding parameters are shown in Table 1. Figure 6c shows Nyquist plots of Pt, NiCo₂S₄, and NiCo₂S₄-an CEs and the insets of Figure 6c are the equivalent circuit and the magnified Nyquist impedance. In the equivalent circuit, R_s represents the series resistance including the sheet resistance of the substrates (FTO and Ti sheet) and the contact resistance of the symmetrical cell, which is mainly correlated to electron transfer rates to the interface of CE/electrolyte and it can be estimated from the intercept on the real axis at the high frequency. The intercept of the middle frequency semicircle on the real axis represents R_{ct} at the interface between CE and electrolyte. The R_{ct} , which is closely related to the electrocatalytic activity and the reaction kinetics of the CE, is an important parameter to determine the FF of cell [36,38,39]. Generally, because of the symmetrical structure, R_{ct1} and R_{ct2} at the two CE/electrolyte interfaces are equal ($R_{ct1} = R_{ct2}$), so every Nyquist plot has one semicircle [35,40]. The obtained impedance spectra are fitted by Z-View software, as shown in Table 1. The R_s values of Pt, NiCo₂S₄ and NiCo₂S₄-an CEs are 8.639 Ω , 3.139 Ω and 3.01 Ω , respectively. Among them, the R_s values of NiCo₂S₄, and NiCo₂S₄-an CEs are close, which may be ascribed to the same Ti-PF substrates. The R_s of Pt CE is much higher than that of NiCo₂S₄ and NiCo₂S₄-an CEs, which is attributed to the strong chemisorption of S²⁻ ions on Pt. R_{ct} directly reflects the electrochemical reaction at CE/electrolyte interface, R_{ct} values of Pt, NiCo₂S₄, and NiCo₂S₄-an CEs are 6860 Ω , 67.47 Ω , and 33.31 Ω , respectively; this means that it is easier for charges transfer through the NiCo₂S₄-an/electrolyte interface than Pt/electrolyte and NiCo₂S₄/electrolyte interfaces. Thus, it is anticipated that the QDSSC with Ti-PF-supported NiCo₂S₄ nanotube CE will show better photovoltaic performance. Furthermore, the proper annealing treatment reduced the R_{ct} of NiCo₂S₄/electrolyte interface and improved the short-circuit photocurrent density (J_{sc}) and PCE of QDSSC.

Table 1. Photovoltaic parameters obtained from J–V curves of quantum-dot-sensitized solar cells (QDSSCs) and EIS parameters of symmetric cells.

Samples	V_{oc} (V)	J_{sc} (mA/cm ²)	FF (%)	PCE (%)	R_s (Ω)	R_{ct} (Ω)
Pt	0.489 (0.483)	11.76 (10.29)	22.56 (25.19)	1.30 (1.21)	8.639	6860
NiCo ₂ S ₄	0.456 (0.45)	13.72 (13.56)	40.60 (40.46)	2.54 (2.51)	3.139	67.47
NiCo ₂ S ₄ -an	0.489 (0.478)	16.68 (15.32)	38.52 (38.61)	3.14 (2.82)	3.010	33.31

Complete photovoltaic cells based on NiCo₂S₄ and NiCo₂S₄-an CEs were fabricated and the cell based on Pt CE is used as the reference. In this study, Pt, NiCo₂S₄, and NiCo₂S₄-a CEs were soaked in S_n²⁻/S²⁻ electrolyte for 24 h and then were used in the complete photovoltaic cells. The complete photovoltaic cells and symmetric cells were fixed by clip and spacer with 90 μm thickness. The photovoltaic curves and the photovoltaic parameters (open-circuit voltage (V_{oc}), J_{sc} , FF, and PCE) are shown in Figure 6d and Table 1, respectively. From Figure 6d, obviously, the performance of QDSSCs based on NiCo₂S₄ and NiCo₂S₄-an CEs are better than that of QDSSC with Pt CE.

The champion QDSSC based on Pt CE has an V_{oc} of 0.489V, a J_{sc} of 11.76 mA/cm², a FF of 22.56%, and a PCE of 1.3%. The champion QDSSC with NiCo₂S₄ CE has a V_{oc} of 0.456V, a J_{sc} of 13.72 mA/cm², a FF of 40.6%, and a PCE of 2.54%. The champion QDSSC employing NiCo₂S₄-an CE has a V_{oc} of 0.489V, a J_{sc} of 16.68 mA/cm², a FF of 38.52%, and a PCE of 3.14%. Notably, the PCE increased from 1.3% to 3.14% when Pt CE was replaced with NiCo₂S₄-an CE. In addition, the average values obtained of the three best cells (up to nine) based on an optimal photoanode and three CEs are given in brackets, as shown in Table 1, and the change trends of the average values of V_{oc} , J_{sc} , FF, and PCE are consistent with the champion QDSSCs. This improvement in the cell performance originates from the significant increases in both J_{sc} and FF, which closely related to the higher electrocatalytic ability of CE. Furthermore, the QDSSC with NiCo₂S₄-an CE shows a higher J_{sc} and V_{oc} than that with NiCo₂S₄ CE and thus obtains a higher PCE. V_{oc} of QDSSC depends upon the difference between the quasi Fermi level of the photoanode and the redox potential of the electrolyte. The annealing treatment improved the crystallinity and the conductivity of NiCo₂S₄, so the fast charge transfer at CE/electrolyte interface can cause a change in the concentration gradient in the electrolyte solution, which influences the recombination rates at the photoanode/electrolyte interface and consequently the conduction band position of the photoanode. Meanwhile, the high conductivity of NiCo₂S₄-an CE also increased the photocurrent of cell [41]. J-V parameters are in line with the electrocatalytic ability of CEs discussed in the CV, Tafel polarization, and EIS.

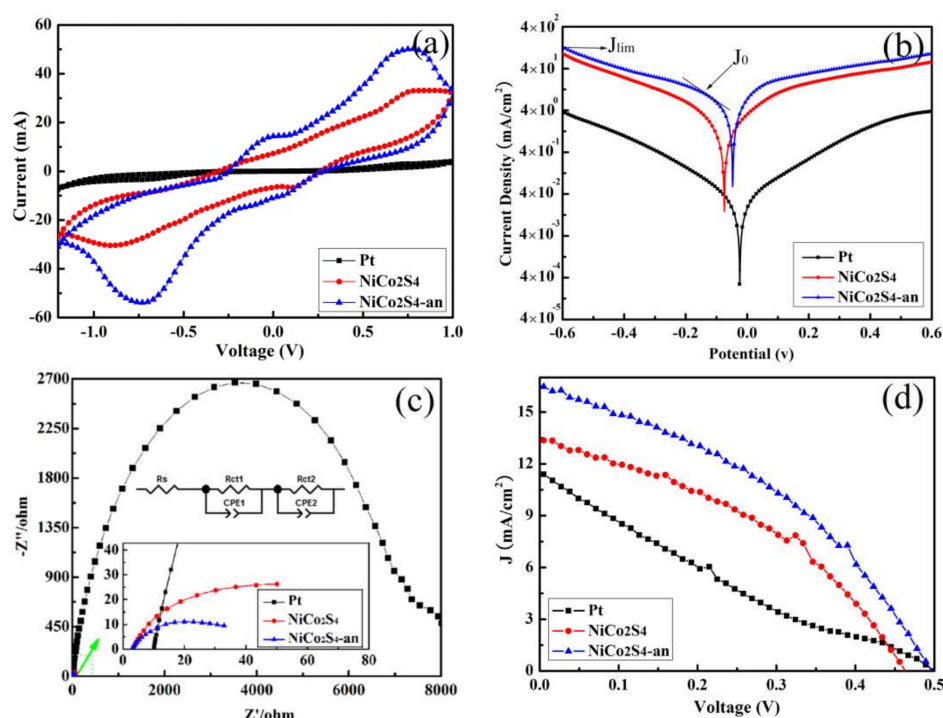


Figure 6. (a) Cyclic voltammetry (CV); (b) Tafel curves; and (c) EIS of the symmetric cells with Pt, NiCo₂S₄, and NiCo₂S₄-an CEs and (d) J-V characteristics for QDSSCs based on Pt, NiCo₂S₄, and NiCo₂S₄-an CEs, respectively.

4. Conclusions

In summary, we have prepared Ti-PF by the acid etching technique and Ti-PF supporting NiCo₂S₄ nanotubes via two-step hydrothermal method; furthermore, Ti-PF supporting NiCo₂S₄ nanotubes are used as CE in QDSSCs. The morphology of Ti-PF is affected with the etching time. When etching time is 48 h in hydrochloric acid with a weight concentration of 25% at room temperature, the holes are uniformly formed on the surface of Ti sheet, which is most suitable for use as the substrate to support CE materials. SEM, TEM, and XRD results show that the as-synthesized NiCo₂S₄ nanotube with porous surface is the cubic phase. Using a polysulfide electrolyte in the symmetric cells, Ti-PF/NiCo₂S₄ CE provided greater electrocatalytic activity (a higher reduction current density, a higher J_0 and J_{lim}) and lower internal resistance (R_s and R_{ct}). Also, Ti-PF/NiCo₂S₄ was used to fabricate QDSSC, it has a higher performance ($J_{sc} = 16.68 \text{ mA/cm}^2$, $V_{oc} = 0.489 \text{ V}$, FF = 38.52%, and PCE = 3.14%) than that based on FTO/Pt CE ($J_{sc} = 11.76 \text{ mA/cm}^2$, $V_{oc} = 0.489 \text{ V}$, FF = 22.56%, and PCE = 1.3%).

Acknowledgments: Scientific Research Project of Education Department of Shaanxi Provincial Government (Grant No. 16JS016), Scientific Research Project of Science and Technology Department of Shaanxi Provincial Government (Grant No. 2014SZS16-K02), Natural Science Foundation of Shaanxi Province (Grant No. 2017JM6090). The authors gratefully acknowledge financial support from Natural Science Foundation of China (Grant Nos. 61176056 and 51572216), the industrial science and technology research project in Shaanxi province (2015GY005), the Key Scientific and Technological Project of Henan Province, China (No. 172102210344), and the Key Program of the Higher Education Institutions of Henan Province in China (grant No. 17A140008).

Author Contributions: Jianping Deng and Minqiang Wang designed the experiments. Jianping Deng and Zhaolin Yuan performed the experiments. Xiaohui Song and Zhi Yang analyzed the data and wrote the paper.

Conflicts of Interest: The authors declare no conflict of interest.

References

1. Deng, J.; Wang, M.; Yang, Z.; Yang, Y.; Zhang, P. Preparation of TiO₂ Nanoparticles Two-Dimensional Photonic-Crystals: A Novel Scattering Layer of Quantum Dot-Sensitized Solar Cells. *Mater. Lett.* **2016**, *183*, 307–310. [[CrossRef](#)]
2. Radich, J.G.; Dwyer, R.; Kamat, P.V. Cu₂S Reduced Graphene Oxide Composite for High-Efficiency Quantum Dot Solar Cells. Overcoming the Redox Limitations of S²⁻/Sn²⁻ at the Counter Electrode. *J. Phys. Chem. Lett.* **2011**, *2*, 2453–2460. [[CrossRef](#)]
3. Wang, H.; Hu, Y.H. Graphene as a Counter Electrode Material for Dye-Sensitized Solar Cells. *Energy Environ. Sci.* **2012**, *5*, 8182–8188. [[CrossRef](#)]
4. Batmunkh, M.; Biggs, M.J.; Shapter, J.G. Carbon Nanotubes for Dye-Sensitized Solar Cells. *Small* **2015**, *11*, 2963–2989. [[CrossRef](#)] [[PubMed](#)]
5. Hwang, S.; Batmunkh, M.; Nine, M.J.; Chung, H.; Jeong, H. ChemPhysChem Dye-Sensitized Solar Cell Counter Electrodes Based on Carbon Nanotubes. *ChemPhysChem* **2015**, *16*, 53–65. [[CrossRef](#)] [[PubMed](#)]
6. Jafari, F.; Behjat, A.; Khoshro, A.R.; Ghoshani, M. A Dye-Sensitized Solar Cell Based on Natural Photosensitizers and a PEDOT:PSS/TiO₂ Film as a Counter Electrode. *Eur. Phys. J. Appl. Phys.* **2015**, *69*, 20502. [[CrossRef](#)]
7. Song, X.; Wang, M.; Deng, J.; Ju, Y.; Xing, T.; Ding, J.; Yang, Z.; Shao, J. ZnO/PbS Core/Shell Nanorod Arrays as Efficient Counter Electrode for Quantum Dot-Sensitized Solar Cells. *J. Power Sources* **2014**, *269*, 661–670. [[CrossRef](#)]
8. Yang, Z.; Chen, C.-Y.; Liu, C.-W.; Li, C.-L.; Chang, H.-T. Quantum Dot-Sensitized Solar Cells Featuring CuS/CoS Electrodes Provide 4.1% Efficiency. *Adv. Energy Mater.* **2011**, *1*, 259–264. [[CrossRef](#)]
9. Geng, H.; Zhu, L.; Li, W.; Liu, H.; Quan, L.; Xi, F.; Su, X. FeS/Nickel Foam as Stable and Efficient Counter Electrode Material for Quantum Dot Sensitized Solar Cells. *J. Power Sources* **2015**, *281*, 204–210. [[CrossRef](#)]
10. Faber, M.S.; Park, K.; Caban-Acevedo, M.; Santra, P.K.; Jin, S. Earth-Abundant Cobalt Pyrite (CoS₂) Thin Film on Glass as a Robust, High-Performance Counter Electrode for Quantum Dot-Sensitized Solar Cells. *J. Phys. Chem. Lett.* **2013**, *4*, 1843–1849. [[CrossRef](#)] [[PubMed](#)]

11. Chen, C.; Ye, M.; Zhang, N.; Wen, X.; Zheng, D.; Lin, C. Preparation of Hollow Co₉S₈ Nanoneedle Arrays as Effective Counter Electrodes for Quantum Dot-Sensitized Solar Cells. *J. Mater. Chem. A* **2015**, *3*, 6311–6314. [[CrossRef](#)]
12. Manjcevan, A.; Bandara, J. Optimization of Performance and Stability of Quantum Dot Sensitized Solar Cells by Manipulating the Electrical Properties of Different Metal Sulfide Counter Electrodes. *Electrochim. Acta* **2017**, *235*, 390–398. [[CrossRef](#)]
13. Xiao, J.; Wan, L.; Yang, S.; Xiao, F.; Wang, S. Design Hierarchical Electrodes with Highly Conductive NiCo₂S₄ Nanotube Arrays Grown on Carbon Fiber Paper for High-Performance Pseudocapacitors. *Nano Lett.* **2014**, *14*, 831–838. [[CrossRef](#)] [[PubMed](#)]
14. Yan, M.; Yao, Y.; Wen, J.; Long, L.; Kong, M.; Zhang, G.; Liao, X.; Yin, G.; Huang, Z. Construction of a Hierarchical NiCo₂S₄@PPy Core-Shell Heterostructure Nanotube Array on Ni Foam for a High-Performance Asymmetric Supercapacitor. *ACS Appl. Mater. Interfaces* **2016**, *8*, 24525–24535. [[CrossRef](#)] [[PubMed](#)]
15. Peng, S.; Li, L.; Li, C.; Tan, H.; Cai, R.; Yu, H.; Mhaisalkar, S.; Srinivasan, M.; Ramakrishna, S.; Yan, Q. In Situ Growth of NiCo₂S₄ Nanosheets on Graphene for High-Performance Supercapacitors. *Chem. Commun.* **2013**, *49*, 10178–10180. [[CrossRef](#)] [[PubMed](#)]
16. Chen, L.; Zhou, Y.; Dai, H.; Yu, T.; Liu, J.; Zou, Z. One-Step Growth of CoNi₂S₄ Nanoribbons on Carbon Fibers as Platinum-Free Counter Electrodes for Fiber-Shaped Dye-Sensitized Solar Cells with High Performance: Polymorph-Dependent Conversion Efficiency. *Nano Energy* **2015**, *11*, 697–703. [[CrossRef](#)]
17. Shi, Z.; Deng, K.; Li, L. Pt-Free and Efficient Counter Electrode with Nanostructured CoNi₂S₄ for Dye-Sensitized Solar Cells. *Sci. Rep.* **2015**, *5*, 9317. [[CrossRef](#)] [[PubMed](#)]
18. Shi, Z.; Lu, H.; Liu, Q.; Cao, F.; Guo, J.; Deng, K.; Li, L. Efficient p-Type Dye-Sensitized Solar Cells with All-Nano-Electrodes: NiCo₂S₄ Mesoporous Nanosheet Counter Electrodes Directly Converted from NiCo₂O₄ Photocathodes. *Nanoscale Res. Lett.* **2014**, *9*, 608. [[CrossRef](#)] [[PubMed](#)]
19. Huo, J.; Wu, J.; Zheng, M.; Tu, Y.; Lan, Z. Flower-Like Nickel Cobalt Sulfide Microspheres Modified with Nickel Sulfide as Pt-Free Counter Electrode for Dye-Sensitized Solar Cells. *J. Power Sources* **2016**, *304*, 266–272. [[CrossRef](#)]
20. Huang, N.; Zhang, S.; Huang, H.; Liu, J.; Sun, Y.; Sun, P.; Bao, C.; Zheng, L.; Sun, X.; Zhao, X. Pt-Sputtering-Like NiCo₂S₄ Counter Electrode for Efficient Dye-Sensitized Solar Cells. *Electrochim. Acta* **2016**, *192*, 521–528. [[CrossRef](#)]
21. Khoo, S.Y.; Miao, J.; Yang, H.; He, Z.; Leong, K.C.; Liu, B.; Thatt, T.; Tan, Y. One-Step Hydrothermal Tailoring of NiCo₂S₄ Nanostructures on Conducting Oxide Substrates as an Efficient Counter Electrode in Dye-Sensitized Solar Cells. *Adv. Mater. Interfaces* **2015**, *2*, 1500384. [[CrossRef](#)]
22. Chen, H.; Jiang, J.; Zhang, L.; Xia, D.; Zhao, Y.; Guo, D.; Qi, T.; Wan, H. In Situ Growth of NiCo₂S₄ Nanotube Arrays on Ni Foam for Supercapacitors: Maximizing Utilization Efficiency at High Mass Loading to Achieve Ultrahigh Areal Pseudocapacitance. *J. Power Sources* **2014**, *254*, 249–257. [[CrossRef](#)]
23. Park, J.T.; Lee, C.S.; Kim, J.H. High Performance Electrocatalyst Consisting of CoS Nanoparticles on an Organized Mesoporous SnO₂ Film: Use as Counter Electrodes for Pt-Free, Dye-Sensitized Solar Cells. *Nanoscale* **2015**, *7*, 670–678. [[CrossRef](#)] [[PubMed](#)]
24. Xu, S.; Luo, Y.; Zhong, W.; Xiao, Z.; Luo, Y.; Ou, H. Nanoporous TiO₂/SnO₂/Poly(3,4-ethylene-dioxythiophene): Polystyrenesulfonate Composites as Efficient Counter Electrode for Dye Sensitized Solar Cells. *J. Nanosci. Nanotechnol.* **2016**, *16*, 392–399. [[CrossRef](#)] [[PubMed](#)]
25. Chen, H.; Zhu, L.; Liu, H.; Li, W. Efficient Iron Sulfide Counter Electrode for Quantum Dots Sensitized Solar Cells. *J. Power Sources* **2014**, *245*, 406–410. [[CrossRef](#)]
26. Du, J.; Du, Z.; Hu, J.-S.; Pan, Z.; Shen, Q.; Sun, J.; Long, D.; Dong, H.; Sun, L.; Zhong, X.; et al. Zn–Cu–In–Se Quantum Dot Solar Cells with a Certified Power Conversion Efficiency of 11.6%. *J. Am. Chem. Soc.* **2016**, *138*, 4201–4209. [[CrossRef](#)] [[PubMed](#)]
27. Yang, Y.; Zhu, L.; Sun, H.; Huang, X.; Luo, Y.; Li, D.; Meng, Q. Composite Counter Electrode Based on Nanoparticulate PbS and Carbon Black: Towards Quantum Dot-Sensitized Solar Cells with Both High Efficiency and Stability. *ACS Appl. Mater. Interfaces* **2012**, *4*, 6162–6168. [[CrossRef](#)] [[PubMed](#)]
28. Fu, W.; Zhao, C.; Han, W.; Liu, Y.; Zhao, H.; Ma, Y.; Xie, E. Cobalt Sulfide Nanosheets Coated on NiCo₂S₄ Nanotube Arrays as Electrode Materials for High-performance Supercapacitors. *J. Mater. Chem. A* **2015**, *3*, 10492–10497. [[CrossRef](#)]

29. Deng, J.; Wang, M.; Zhang, P.; Ye, W. Preparing ZnO Nanowires in Mesoporous TiO₂ Photoanode by an in-Situ Hydrothermal Growth for Enhanced Light-Trapping in Quantum Dots-Sensitized Solar Cells. *Electrochim. Acta* **2016**, *200*, 12–20. [[CrossRef](#)]
30. Li, R.; Wang, S.; Huang, Z.; Lu, F.; He, T. NiCo₂S₄@Co(OH)₂ Core-Shell Nanotube Arrays in Situ Grown on Ni Foam for High Performances Asymmetric Supercapacitors. *J. Power Sources* **2016**, *312*, 156–164. [[CrossRef](#)]
31. Park, J.; Zheng, H.; Jun, Y.; Alivisatos, A.P. Hetero-Epitaxial Anion Exchange Yields Single-Crystalline Hollow Nanoparticles. *J. Am. Chem. Soc.* **2009**, *131*, 13943–13945. [[CrossRef](#)] [[PubMed](#)]
32. Lu, F.; Zhou, M.; Li, W.; Weng, Q.; Li, C.; Xue, Y.; Jiang, X.; Zeng, X.; Bando, Y.; Golberg, D. Engineering Sulfur Vacancies and Impurities in NiCo₂S₄ Nanostructures Toward Optimal Supercapacitive Performance. *Nano Energy* **2016**, *26*, 313–323. [[CrossRef](#)]
33. Su, A.-L.; Lu, M.-N.; Chang, C.-Y.; Wei, T.-C.; Lin, J.-Y. Scalable Fabrication of Efficient NiCo₂S₄ Counter Electrodes for Dye-sensitized Solar Cells Using a Facile Solution Approach. *Electrochim. Acta* **2016**, *222*, 1410–1416. [[CrossRef](#)]
34. Du, F.; Yang, Q.; Qin, T.; Li, G. Morphology-Controlled Growth of NiCo₂O₄ Ternary Oxides and Their Application in Dye-Sensitized Solar Cells as Counter Electrodes. *Sol. Energy* **2017**, *146*, 125–130. [[CrossRef](#)]
35. Wang, S.; Dong, W.; Fang, X.; Zhou, S.; Shao, J.; Deng, Z.; Tao, R.; Zhang, Q.; Hu, L.; Zhu, J. Enhanced Electrocatalytic Activity of Vacuum Thermal Evaporated Cu_xS Counter Electrode for Quantum Dot-Sensitized Solar Cells. *Electrochim. Acta* **2015**, *154*, 47–53. [[CrossRef](#)]
36. Dennyson Savariraj, A.; Viswanathan, K.K.; Prabakar, K. CuS Nano-flakes and Nano-platelets as Counter Electrode for Quantum Dots Sensitized Solar Cells. *Electrochim. Acta* **2014**, *149*, 364–369. [[CrossRef](#)]
37. Zakeeruddin, S.M.; Gratzel, M. Solvent-Free Ionic Liquid Electrolytes for Mesoscopic Dye Sensitized Solar Cells. *Adv. Funct. Mater.* **2009**, *19*, 2187–2202. [[CrossRef](#)]
38. Meng, K.; Surolia, P.K.; Byrne, O.; Thampi, K.R. Efficient CdS Quantum Dot Sensitized Solar Cells Made Using Novel Cu₂S Counter Electrode. *J. Power Sources* **2014**, *248*, 218–223. [[CrossRef](#)]
39. Li, D.-M.; Cheng, L.-Y.; Zhang, Y.-D.; Zhang, Q.-X.; Huang, X.-M.; Luo, Y.-H.; Meng, Q.-B. Development of Cu₂S/Carbon Composite Electrode for CdS/CdSe Quantum Dot Sensitized Solar Cell Modules. *Sol. Energy Mater. Sol. C* **2014**, *120*, 454–461. [[CrossRef](#)]
40. Liberatore, M.; Decker, F.; Burtone, L.; Zardetto, V.; Brown, T.M.; Reale, A.; Di Carlo, A. Using EIS for Diagnosis of Dye-Sensitized Solar Cells Performance. *J. Appl. Electrochem.* **2009**, *39*, 2291. [[CrossRef](#)]
41. Liu, F.; Zhu, J.; Li, Y.; Wei, J.; Lv, M.; Xu, Y.; Zhou, L.; Hu, L.; Dai, S. Earth-Abundant Cu₂SnSe₃ Thin Film Counter Electrode for High Efficiency Quantum Dot-Sensitized Solar Cells. *J. Power Sources* **2015**, *292*, 7–14. [[CrossRef](#)]

